

Influences of Alkaline Earth Metal Substitution on the Crystal Structure and Physical Properties of Magnetic $\text{RuSr}_{1.9}\text{A}_{0.1}\text{GdCu}_2\text{O}_8$ (A = Ca, Sr, and Ba) Superconductors

Su Gil Hur, Dae Hoon Park, and Seong-Ju Hwang*

Center for Intelligent Nano-Bio Materials (CINBM), Division of Nano Sciences and Department of Chemistry, Ewha Womans University, Seoul 120-750, Korea

Seung Joo Kim

Department of Chemistry, College of Natural Sciences, Ajou University, Gyunggi 443-749, Korea

J. H. Lee and Sang Young Lee

Department of Physics and Department of Advanced Technology Fusion, Center for Emerging Wireless Transmission Technology, Konkuk University, Seoul 143-701, Korea

Received: August 23, 2005; In Final Form: September 15, 2005

We have investigated the effect of alkaline earth metal substitution on the crystal structure and physical properties of magnetic superconductors $\text{RuSr}_{1.9}\text{A}_{0.1}\text{GdCu}_2\text{O}_8$ (A = Ca, Sr, and Ba) in order to probe an interaction between the magnetic coupling of the RuO_2 layer and the superconductivity of the CuO_2 layer. X-ray diffraction and X-ray absorption spectroscopic analyses demonstrate that the isovalent substitution of Sr ions with Ca or Ba ions makes it possible to tune the interlayer distance between the CuO_2 and the RuO_2 layers. From the measurements of electrical resistance and magnetic susceptibility, it was found that, in contrast to negligible change of magnetization, both of the alkaline earth metal substitutions lead to a notable depression of zero-resistance temperature T_c ($\Delta T_c \sim 17\text{--}19$ K). On the basis of the absence of a systematic correlation between the T_c and the interlayer distance/magnetization, we have concluded that the internal magnetic field of the RuO_2 layer has insignificant influence on the superconducting property of the CuO_2 layer in the ruthenocuprate.

Introduction

Recently ruthenocuprates $\text{RuSr}_2\text{LnCu}_2\text{O}_8$ (Ln = Gd, Eu) have attracted intense research interest due to the coexistence of superconductivity and ferromagnetism. These materials are of special importance as model compounds for studying the effect of intrinsic magnetic field on the superconducting properties of layered copper oxides.^{1–3} In this regard, there have been many research activities devoted to their physicochemical properties such as spin alignment and interaction, superconductivity, crystal and electronic structures, and so on.^{3–13} These magnetic superconductors were reported to show a weak ferromagnetism or an antiferromagnetism depending on the strength of applied magnetic field.^{3,6–10} The presence of the weak ferromagnetism in RuO_2 layer originates from the canting of antiferromagnetically ordered Ru moments. Such a magnetic coupling of Ru moments has been reported to induce a pair-breaking effect on the superconductive CuO_2 layer, resulting in frustration of superconductivity.^{3–6} However, there has been no direct experimental evidence on the interplay between magnetic coupling and superconductivity in these magnetic superconductors. In addressing this issue, it would be very informative to examine the relationship between the crystal structure and the superconducting properties. The control of crystal structure and physical properties could be achieved by chemical substitution. Recently we have prepared La-substituted $\text{RuSr}_{2-x}\text{La}_x\text{GdCu}_2\text{O}_8$ com-

pounds and found that the replacement of Sr^{II} with La^{III} leads to the decrease of the hole density in the CuO_2 layer and the variation of magnetic coupling in the RuO_2 layer.¹⁴ In this regard, the observed depression of zero-resistance temperature (T_c) upon the La substitution was interpreted to be due to the change of the electronic and/or magnetic structures caused by an electron doping.^{14,15} In that system with varied hole density, it is still difficult to directly probe the effects of crystal structure and internal magnetic field on the superconductivity of the ruthenocuprate.

In this work, we have synthesized alkaline earth metal-substituted $\text{RuSr}_{1.9}\text{A}_{0.1}\text{GdCu}_2\text{O}_8$ (A = Ca, Sr, and Ba) ruthenocuprates, since the different ionic sizes of the alkaline earth metal substituent allow us to control the interlayer distance and magnetic interaction between the CuO_2 and the RuO_2 layers. Evolutions of the superconducting and magnetic properties upon Ca or Ba substitution have been examined by measuring direct current (dc) electrical resistance and dc magnetization measurements. Also, we have carried out X-ray diffraction (XRD) and X-ray absorption spectroscopic (XAS) analyses to investigate the effect of the alkaline earth metal substitution on the crystal and electronic structures of the pristine ruthenocuprate.

Experimental Section

The polycrystalline samples of $\text{RuSr}_{1.9}\text{A}_{0.1}\text{GdCu}_2\text{O}_8$ (A = Ca, Sr, and Ba) were synthesized by a conventional solid-state reaction with prolonged heat treatments in argon and oxygen atmosphere, as reported earlier.⁴ The formation of the perovskite-

* To whom all correspondences should be addressed. Telephone: +82-2-3277-4370. Fax: +82-2-3277-3419. E-mail: hwangsj@ewha.ac.kr.

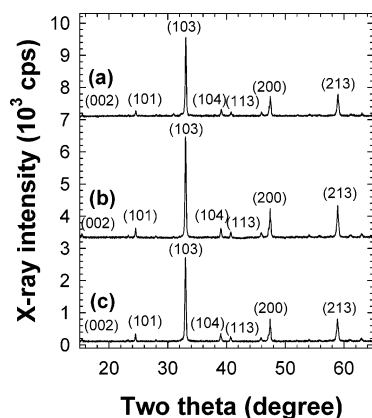


Figure 1. Powder XRD patterns of the alkaline earth metal substituted $\text{RuSr}_{1.9}\text{A}_{0.1}\text{GdCu}_2\text{O}_8$ with A = (a) Ca, (b) Sr, and (c) Ba. Each pattern is shifted along the y-axis for the clarity.

structured ruthenocuprates was confirmed by XRD measurements using Ni-filtered Cu K α radiation with a graphite diffracted beam monochromator. The morphology and particle size of the ruthenocuprates were examined with field emission-scanning electron microscopy (FE-SEM). Semiquantitative energy-dispersive spectroscopic (EDS) microprobe analysis was carried out on several crystallites, confirming successful incorporation of Ca or Ba into the lattice of the ruthenocuprate. The electrical resistivity and the magnetic property of the present samples were probed by performing the dc resistance and the dc magnetization measurements, respectively. XAS experiments were carried out at Cu K- and Ru K-edges by using the extended X-ray absorption fine structure (EXAFS) facility installed at the beam line 7C at the Pohang Light Sources (PLS) in Korea, operated at 2.5 GeV and 180 mA. XAS data were collected at room temperature in a transmission mode using gas-ionization detectors. All the present spectra were calibrated carefully by measuring the reference spectra of Cu metal and RuO_2 . Data analysis for the experimental spectra was performed by using the standard procedure.¹⁶ In the course of EXAFS fitting analysis, the coordination number (CN) was fixed to the crystallographic values while the amplitude reduction factor (S_0^2) was allowed to vary. Also, all the bond distances (R), Debye-Waller factors (σ^2), and energy shifts (ΔE) were set as variables. Due to the limitation in the numbers of allowed variables, we have kept the energy shift the same for two (Cu–O) shells at ~ 1.90 – 2.20 Å and two (Ru–O) shells at ~ 1.91 – 1.97 Å, respectively. Such constraints can be rationalized from the fact that the adjacent shells consisting of the same types of atoms would possess a very similar degree of energy shift.

Results and Discussion

Figure 1 represents powder XRD patterns for the pristine $\text{RuSr}_2\text{GdCu}_2\text{O}_8$ and its Ca- and Ba-substituted derivatives. All of the intense diffraction peaks can be well indexed on the basis of the tripled perovskite structure with tetragonal symmetry.⁴ The structure of $\text{RuSr}_2\text{GdCu}_2\text{O}_8$ is that of an oxygen-deficient tripled perovskite cell, consisting of a layer of RuO_6 octahedra connected through their apexes to two layers of CuO_5 square pyramids. A mismatch between the in-plane Ru–O and Cu–O bonds leads to rotations of the RuO_6 octahedra around the c -axis. In the present XRD patterns, we cannot observe any traces of reflections corresponding to a ferromagnetic SrRuO_3 impurity phase. Upon the Ca and Ba substitutions, overall Bragg reflections shift toward high- and low-angle sides, respectively. From Rietveld refinement analyses, the unit cell volume is found

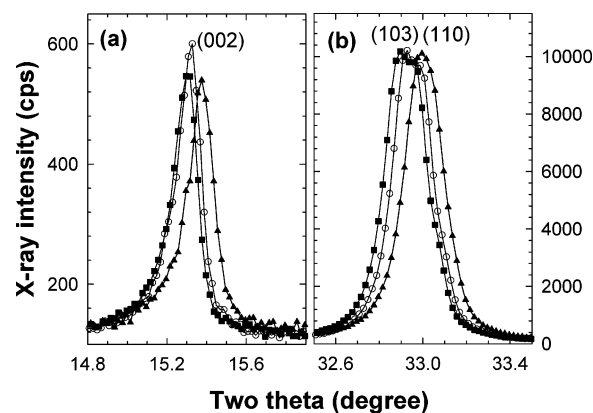


Figure 2. Relative intensities of (a) the (002) peak for $\text{RuSr}_{1.9}\text{A}_{0.1}\text{GdCu}_2\text{O}_8$ with A = Ca (triangles), Sr (circles), and Ba (squares) after normalization with respect to (b) the (103)(110) main peaks.

to slightly decrease upon Ca substitution, whereas the replacement of Sr with Ba causes expansion of the unit cell.¹⁷ It is in good agreement with the relative ionic size of alkaline earth metal ($\text{Ca}^{II}(12) = 1.48$ Å, $\text{Sr}^{II}(12) = 1.58$ Å, and $\text{Ba}^{II}(12) = 1.75$ Å, where the number in parentheses represents the coordination number).¹⁸ In the case of the tripled perovskites $\text{RuSr}_{1.9}\text{A}_{0.1}\text{GdCu}_2\text{O}_8$ (A = Ca, Sr, and Ba), the cation disorder that arises from the c/a ratio being very close to 3 is also important. The c/a ratios are determined to be 2.997 for $\text{RuSr}_{1.9}\text{Ca}_{0.1}\text{GdCu}_2\text{O}_8$ and 3.017 for $\text{RuSr}_{1.9}\text{A}_{0.1}\text{GdCu}_2\text{O}_8$ (A = Sr and Ba), respectively.¹⁷ Compared with simple disordered primitive perovskite ($c/a = 1$), tripled perovskite shows additional superlattice peaks in XRD patterns, from which the degree of ordering can be determined. In particular, intensities of (00*l*) peaks ($l \neq 3n$) are strongly related to the ordering degree along the c -axis. In the perfectly ordered structure, the (002) peak for the Ca-doped sample is expected to be stronger than that of the undoped sample because of the increase in the difference of X-ray scattering factors of Sr(Ca)/Gd compared to that of Sr/Gd. As shown in Figure 2, however, relative intensities of the (002) peaks for both the Ca- and the Ba-doped samples are slightly weaker than that of the undoped sample. The XRD data suggest strongly the structural disorder due to partial occupation of Ca in the Gd site (in this case some Gd atoms are pushed out to Sr sites) and/or of Cu in the Ru site for the Ca-doped sample. Such cation mixing is surely due to the similar size of Gd^{III} and Ca^{II} ions ($\text{Gd}^{III}(8) = 1.193$ Å and $\text{Ca}^{II}(8) = 1.26$ Å, where the number in parentheses represents the coordination number).¹⁸ The much larger sizes of Sr^{II} and Ba^{II} ions ($\text{Sr}^{II}(8) = 1.40$ Å and $\text{Ba}^{II}(8) = 1.56$ Å) prevent them from introducing into Gd site, leading to no existence of the cation disorder in the pristine $\text{RuSr}_2\text{GdCu}_2\text{O}_8$ and its Ba-substituted derivative.

We have examined the morphology and particle size of the ruthenocuprates with FE-SEM. As shown in Figure 3, the pristine $\text{RuSr}_2\text{GdCu}_2\text{O}_8$ and its substituted derivatives display commonly a platelike morphology consisting of a stack of layered crystallites, which accords well with the high structural anisotropy of the ruthenocuprates. The particle size of all the present compounds ranges from ~ 1 to 5 μm , indicating little influence of the alkaline earth metal substitution on the crystal growth of the ruthenocuprate.

The normalized electrical resistivity of $\text{RuSr}_{1.9}\text{A}_{0.1}\text{GdCu}_2\text{O}_8$ (A = Ca, Sr, and Ba) was measured as a function of temperature to examine the effect of the alkaline earth metal substitution on the superconducting and electrical transport properties of the ruthenocuprates. As plotted in Figure 4, the T_c is observed at 31.8 K for the pristine compound, whereas the alkaline earth

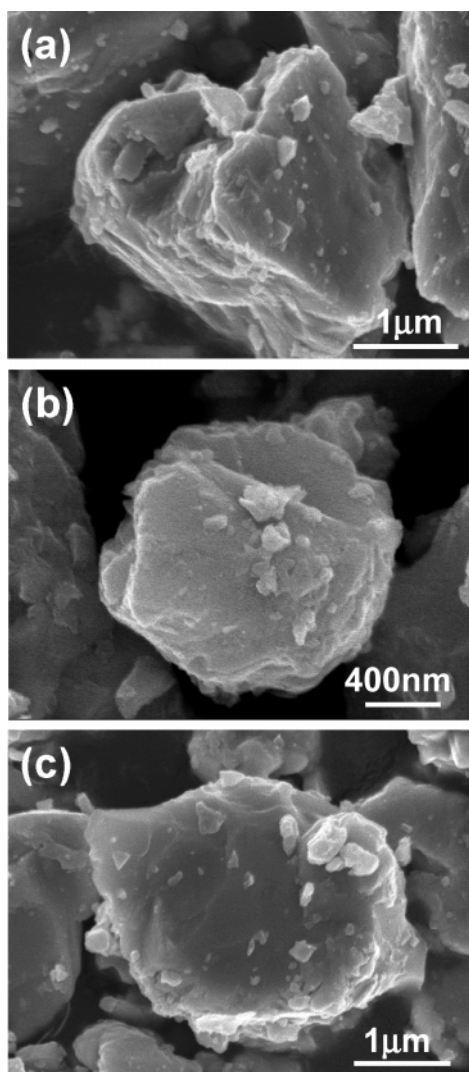


Figure 3. FE-SEM images for the alkaline earth metal substituted $\text{RuSr}_{1.9}\text{A}_{0.1}\text{GdCu}_2\text{O}_8$ with $\text{A} =$ (a) Ca, (b) Sr, and (c) Ba.

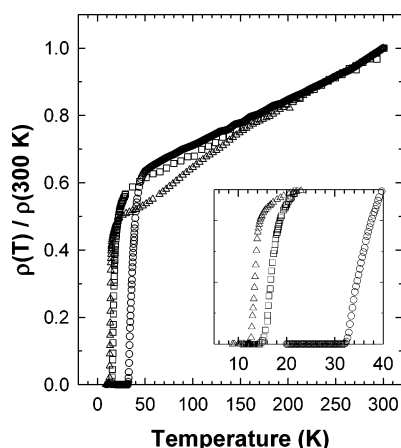


Figure 4. Normalized electrical resistivity $\rho(T)/\rho(300 \text{ K})$ vs temperature plots for $\text{RuSr}_{1.9}\text{A}_{0.1}\text{GdCu}_2\text{O}_8$ with $\text{A} =$ Ca (triangles), Sr (circles), and Ba (squares). Here $\rho(T)$ and $\rho(300 \text{ K})$ denote the electrical resistivity at the measured temperature T and at 300 K, respectively. Inset: Enlarged views of $\rho(T)/\rho(300 \text{ K})$ vs temperature plots for a temperature range of 5–40 K.

metal substitution lowered the T_c to 12.5 K for the Ca-substituted derivative and to 14.5 K for the Ba-substituted one. In contrast to the notable T_c change, the temperature dependence of the normal-state resistivity does not vary significantly before and

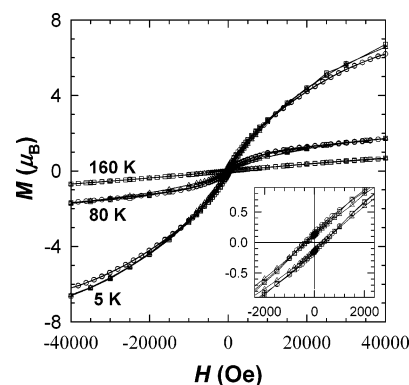


Figure 5. Magnetization (M) vs applied field (H) plots measured at 5–160 K for $\text{RuSr}_{1.9}\text{A}_{0.1}\text{GdCu}_2\text{O}_8$ with $\text{A} =$ Ca (triangles), Sr (circles), and Ba (squares). Inset: Enlarged views of M vs H plots for an applied field range of -2400 to $+2400$ Oe.

after the substitution, implying little modification of the electronic structure. That is, all of the present compounds show almost linear temperature dependence of the resistivity above the onset critical temperature, indicative of their metallic characters.

The effect of alkaline earth metal substitution on the magnetic properties of the ruthenocuprates was investigated with a superconducting quantum interference device (SQUID) magnetometer, as shown in Figure 5. It was found that the coupling behavior of Ru moments remained nearly unchanged before and after the alkaline earth metal substitution. A closer inspection on the magnetization data at 5 K unfolds an insignificant change of coercive field (H_{co}) and remanent magnetization (M_r) below the magnetic transition temperature upon the alkaline earth metal substitution. This observation is in contrast to the marked variation of the magnetization magnitude caused by La substitution.^{14,15} Since the magnetic properties of the ruthenocuprates are sensitive to the oxidation state of Ru ions, the present finding suggests that the isovalent substitution with Ca or Ba has little influence on the valence state of ruthenium ion and the magnetic structure of RuO_2 layers.

We have examined changes in the electronic structures of the CuO_2 and the RuO_2 layers upon the alkaline earth metal substitution by performing X-ray absorption near-edge structure (XANES) analyses at Cu K- and Ru K-edges. Figure 6 displays the Cu K-edge XANES spectra for $\text{RuSr}_{1.9}\text{A}_{0.1}\text{GdCu}_2\text{O}_8$ ($\text{A} =$ Ca, Sr, and Ba), together with those for the references of $\text{La}_2\text{Cu}^{\text{II}}\text{O}_4$ and $\text{LaCu}^{\text{III}}\text{O}_3$. The edge energies of the ruthenocuprates are lower than that of the Cu^{III} reference but slightly higher than that of Cu^{II} one, indicating the mixed oxidation state of copper ($\text{Cu}^{\text{II}}/\text{Cu}^{\text{III}}$) in these compounds. However, the presence of several fine features near a main-edge jump makes it difficult to quantitatively determine the Cu oxidation state from the degree of edge shift. A small preedge peak P appears commonly for all the compounds under investigation, which is due to the quadruple-allowed transition from the core 1s level to an unoccupied 3d state.¹⁹ The position of this peak provides a quantitative measure for the oxidation state of copper. As can be seen clearly from the inset of Figure 6, an enhanced formal valence from Cu^{II} to Cu^{III} leads to an increase of the peak energy by 1.1–1.2 eV. In light of this, the average Cu oxidation state of $\text{RuSr}_2\text{GdCu}_2\text{O}_8$ was estimated to be about +2.09, confirming the hole-underdoped state of this superconductor. Before and after the alkaline earth metal substitution, there is no distinct shift of the preedge peak, indicative of little change in hole density. In the main-edge region, the ruthenocuprates and the reference $\text{La}_2\text{Cu}^{\text{II}}\text{O}_4$ exhibit three features A, B, and C, which

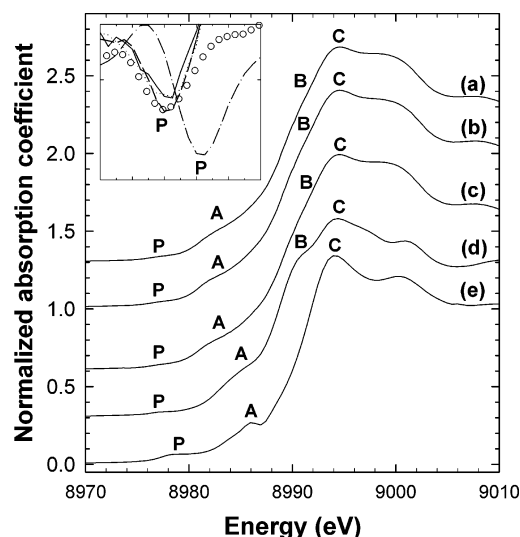


Figure 6. Cu K-edge XANES spectra for $\text{RuSr}_{1.9}\text{A}_{0.1}\text{GdCu}_2\text{O}_8$ with $\text{A} =$ (a) Ca (solid lines), (b) Sr (dashed lines), and (c) Ba (dotted lines), compared with those for (d) La_2CuO_4 (circles) and (e) LaCuO_3 (dotted-dashed lines). Each spectrum is shifted along the y-axis for clarity. Descriptions in parentheses are for the data in the inset. Inset: An enlarged view of the second derivative spectra for an energy range of 8975–8980 eV.

correspond to the dipole-allowed transitions from the core $1s$ level to unoccupied $4p$ states. While peaks A and B are attributable to the transitions from the $1s$ orbital to the out-of-plane $4p_z$ one with and without shakedown processes, respectively, the peak C is ascribed to an in-plane $4p_x$ orbital transition without shakedown process.¹⁹ On the basis of the present assignment, we are able to regard the observation of the separated peaks B and C as evidence for Jahn–Teller distortion around the divalent copper ion with the splitting of degenerate p orbitals. Meanwhile, the reference LaCuO_3 with regular CuO_6 octahedra exhibits only two peaks A and C corresponding to the $1s \rightarrow 4p$ transitions with and without shakedown processes, respectively. The regular octahedral symmetry of CuO_6 in this compound makes the $4p$ orbitals of copper degenerated, leading to the absence of peak splitting of B and C. With a reference to such different origins of the peak C for LaCuO_3 and La_2CuO_4 , it is understandable that the peak C for the higher valent LaCuO_3 has slightly lower energy than that for the lower valent La_2CuO_4 . Instead, the feature C in LaCuO_3 has higher energy by ~ 1.5 eV than the average position of the peaks B and C in La_2CuO_4 .

The Ru K-edge XANES spectra for $\text{RuSr}_{1.9}\text{A}_{0.1}\text{GdCu}_2\text{O}_8$ ($\text{A} = \text{Ca}, \text{Sr}, \text{and Ba}$) are presented in Figure 7, along with the reference spectra for $\text{SrRu}^{\text{IV}}\text{O}_3$, $\text{Ru}^{\text{IV}}\text{O}_2$, and $\text{Sr}_2(\text{Ru}^{\text{V}}_{0.5}\text{Gd}_{0.5})\text{O}_4$. The edge energies of the ruthenocuprates appear higher than those of Ru^{IV} in $\text{SrRu}^{\text{IV}}\text{O}_3$ and $\text{Ru}^{\text{IV}}\text{O}_2$, while being slightly lower than that of Ru^{V} in $\text{Sr}_2(\text{Ru}^{\text{V}}_{0.5}\text{Gd}_{0.5})\text{O}_4$. A comparison of the edge energy between the ruthenocuprates and the Ru^{IV} - and Ru^{V} -containing references allows us to determine the Ru oxidation state of $\text{RuSr}_{1.9}\text{A}_{0.1}\text{GdCu}_2\text{O}_8$ as ~ 4.76 , providing evidence for the mixed oxidation state of ruthenium ($\text{Ru}^{\text{IV}}/\text{Ru}^{\text{V}}$) in the compounds. Upon the alkaline earth metal substitution, there is no detectable shift of an edge jump, indicating little change of the Ru oxidation state. This result accords well with the negligible variation of the magnetization value.

Also, we have carried out Cu K- and Ru K-edge EXAFS analyses to probe the variation of local atomic arrangement around copper and ruthenium ions upon the alkaline earth metal substitution. The k^3 -weighted Cu K-edge EXAFS spectra for

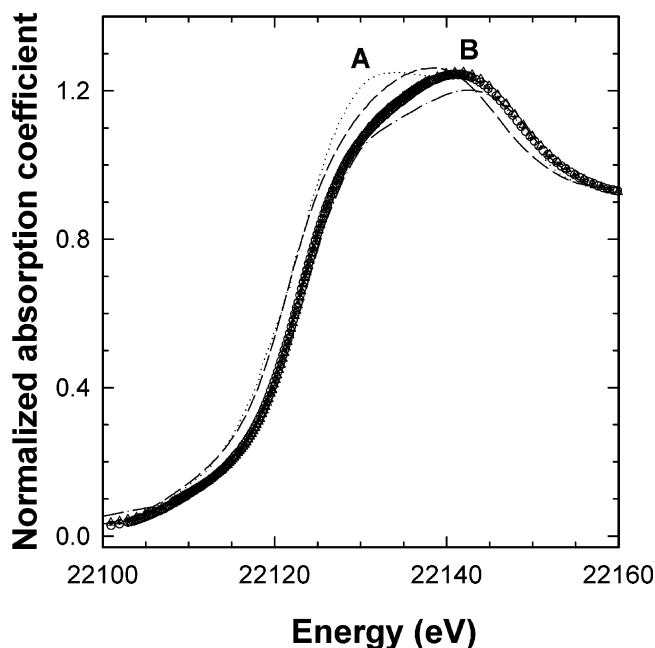


Figure 7. Ru K-edge XANES spectra for $\text{RuSr}_{1.9}\text{A}_{0.1}\text{GdCu}_2\text{O}_8$ with $\text{A} = \text{Ca}$ (dashed lines), Sr (solid lines), and Ba (dotted-dashed lines), $\text{Ru}^{\text{IV}}\text{O}_2$ (circles), $\text{SrRu}^{\text{IV}}\text{O}_3$ (triangles), and $\text{Sr}_2(\text{Ru}^{\text{V}}_{0.5}\text{Gd}_{0.5})\text{O}_4$ (squares).

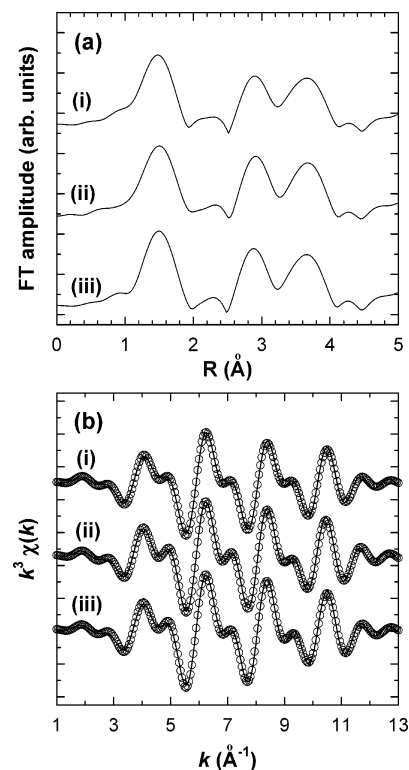


Figure 8. (a) Fourier transformed and (b) Fourier-filtered Cu K-edge EXAFS data for $\text{RuSr}_{1.9}\text{A}_{0.1}\text{GdCu}_2\text{O}_8$ with $\text{A} =$ (i) Ca, (ii) Sr, and (iii) Ba. Each pattern is shifted along the y-axis for clarity. The open circles and the solid lines represent the experimental data and the calculated ones, respectively.

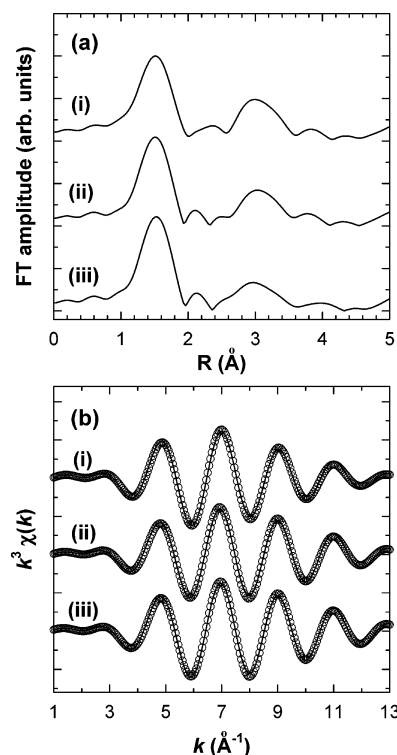
the ruthenocuprate $\text{RuSr}_{1.9}\text{A}_{0.1}\text{GdCu}_2\text{O}_8$ ($\text{A} = \text{Ca}, \text{Sr}, \text{and Ba}$) were Fourier transformed (FT) in the k range of $3.6\text{--}11.2 \text{ \AA}^{-1}$ as shown in Figure 8a. In the FT diagrams, the ruthenocuprate exhibits several intense peaks at ~ 1.5 , ~ 2.4 , ~ 2.9 , and $\sim 3.7 \text{ \AA}$, which are attributed to (Cu–O), (Cu–Gd), (Cu–Cu/Sr/A), and (Cu–Ru) shells, respectively. For quantitative analysis for the variation of the bond distances, the first three FT peaks were

TABLE 1: Results from Nonlinear Least-Squares Fits for the Cu K-Edge EXAFS Spectra for $\text{RuSr}_{1.9}\text{A}_{0.1}\text{GdCu}_2\text{O}_8$ with A = Ca, Sr, and Ba, Respectively

sample	bond	CN	R (Å)	σ^2 (10^{-3} Å ²)
$\text{RuSr}_{1.9}\text{Ca}_{0.1}\text{GdCu}_2\text{O}_8^a$	Cu–O _{eq}	4	1.90	6.13
	Cu–O _{ax}	1	2.18	10.81
	Cu–Gd	4	3.13	8.31
	Cu–Sr/Ca	4	3.25	24.91
$\text{RuSr}_2\text{GdCu}_2\text{O}_8^b$	Cu–O _{eq}	4	1.91	5.13
	Cu–O _{ax}	1	2.23	5.48
	Cu–Gd	4	3.14	7.32
	Cu–Sr	4	3.23	15.99
$\text{RuSr}_{1.9}\text{Ba}_{0.1}\text{GdCu}_2\text{O}_8^c$	Cu–O _{eq}	4	1.92	6.83
	Cu–O _{ax}	1	2.25	4.62
	Cu–Gd	4	3.11	7.62
	Cu–Sr/Ba	4	3.27	24.66

^a The curve-fit was performed for the range of $R = 1.074\text{--}3.16$ Å and $k = 3.60\text{--}11.20$ Å^{−1}. ^b The curve-fit was performed for the range of $R = 1.043\text{--}3.16$ Å and $k = 3.60\text{--}11.20$ Å^{−1}. ^c The curve-fit was performed for the range of $R = 1.043\text{--}3.16$ Å and $k = 3.60\text{--}11.25$ Å^{−1}.

isolated by the inverse FT to k space. The resulting $k^3\chi(k)$ Fourier filtered EXAFS oscillations are represented in Figure 8b, and the curve fittings were carried out on them in order to determine structural parameters such as the coordination number (CN), the bond length (R), and the Debye–Waller factor (σ^2). The best fitting results are compared to the experimental spectra in Figure 8b, and the fitted structural parameters are listed in Table 1.²⁰ The out-of-plane Cu–O_{ax} bond distance decreases upon Ca substitution, whereas the replacement of Sr with bigger Ba leads to the elongation of the axial Cu–O_{ax} bond. In contrast to the minute change of the in-plane Cu–O_{eq} bond length, the variation of the out-of-plane Cu–O_{ax} bond distance upon the substitution is greater than the error range for the estimated bond length ($\Delta R \sim \pm 0.01$ Å). The present findings highlight that the unit cell dimension of the ruthenocuprate along the c -axis can be controlled by the isovalent substitution with alkaline earth metal, as suggested from the variation of lattice parameters.¹⁷ It is worthwhile to note here that the Ca substitution induces a quite prominent change in the Cu–O_{ax} bond distance even at the present low substitution rate. As described above, a detailed comparison of the normalized XRD intensity of the (002) reflection suggested the presence of cationic disorder between Cu and Ru and/or between Ca and Gd sites in the Ca-substituted derivative (Figure 2). In the case in which a fraction of copper ions exist in the Ru site with the out-of-plane Ru–O_{ax} bond distance of 1.92 Å, the Cu_{Ru-site}–O_{ax} bond distance would be much shorter than the Cu_{Cu-site}–O_{ax} bond distance (i.e. 2.23 Å). Therefore, a notable shortening of the average Cu–O_{ax} bond distance upon Ca substitution can be regarded as other evidence of the presence of cationic disorder between the Cu and the Ru sites. From the viewpoint of the bond valence sum concept, the elongation of the axial Cu–O bond distance upon the Ba substitution implies a slight hole depletion while the Cu–O bond shrinkage after Ca substitution corresponds to a minute increase of the hole density. This seems not to be compatible with the negligible shift of the Cu K-edge position. However, it was well-established that the variation of the Cu–O bond distance is more sensitive to the change of the Cu oxidation state than the shift of XANES features.¹⁶ On the other hand, we have found that the Debye–Waller factor of the Cu–O_{ax} shell is much greater for the Ca-substituted compound than the other ruthenocuprates. Such a prominent increase of the factor provides strong evidence of an enhanced structural disorder around the copper ions caused by the Ca substitution. Among the present coordination shells, the Cu–Sr/A shell has the largest Debye–Waller factors, which

**Figure 9.** (a) Fourier transformed and (b) Fourier-filtered Ru K-edge EXAFS data for $\text{RuSr}_{1.9}\text{A}_{0.1}\text{GdCu}_2\text{O}_8$ with A = (i) Ca, (ii) Sr, and (iii) Ba. Each pattern is shifted along the y-axis for clarity. The open circles and the solid lines represent the experimental data and the calculated ones, respectively.**TABLE 2: Results from Nonlinear Least-Squares Fits for the Ru K-Edge EXAFS Spectra for $\text{RuSr}_{1.9}\text{A}_{0.1}\text{GdCu}_2\text{O}_8$ with A = Ca, Sr, and Ba, Respectively**

sample	bond	CN	R (Å)	σ^2 (10^{-3} Å ²)
$\text{RuSr}_{1.9}\text{Ca}_{0.1}\text{GdCu}_2\text{O}_8^a$	Ru–O _{ax}	2	1.92	3.99
	Ru–O _{eq}	4	1.98	5.40
$\text{RuSr}_2\text{GdCu}_2\text{O}_8^b$	Ru–O _{ax}	2	1.92	1.68
	Ru–O _{eq}	4	1.98	3.28
$\text{RuSr}_{1.9}\text{Ba}_{0.1}\text{GdCu}_2\text{O}_8^c$	Ru–O _{ax}	2	1.92	1.81
	Ru–O _{eq}	4	1.98	2.66

^a The curve-fit was performed for the range of $R = 0.920\text{--}1.902$ Å and $k = 4.25\text{--}12.20$ Å^{−1}. ^b The curve-fit was performed for the range of $R = 0.951\text{--}1.902$ Å and $k = 4.20\text{--}12.05$ Å^{−1}. ^c The curve-fit was performed for the range of $R = 0.920\text{--}1.871$ Å and $k = 4.20\text{--}12.10$ Å^{−1}.

is attributable to the tilting of RuO_6 octahedra with respect to the c -axis and the resultant splitting of the Cu–Sr/A bond distances. Moreover, as a result of the partial replacement of Sr ions with Ca or Ba ions, this value is found to be greater for the Ca- or Ba-substituted compounds than for the unsubstituted compound.

Parts a and b of Figure 9 represent the FT data of Ru K-edge EXAFS spectra for the ruthenocuprates $\text{RuSr}_{1.9}\text{A}_{0.1}\text{GdCu}_2\text{O}_8$ (A = Ca, Sr, and Ba) and the corresponding inverse FT spectra, respectively. There are two intense peaks at ~ 1.5 and ~ 3.1 Å in all of the present FT data of the ruthenocuprates, which originate from Ru–O and Ru–Sr/A shells, respectively. To determine the variation in the bond distances of Ru–O, the first FT peak was isolated by the inverse FT to k space and then curve-fitted. The results from the best fit are compared to the experimental spectra in Figure 9b, and the fitted structural parameters are summarized in Table 2.²¹ The alkaline earth metal substitution does not cause significant change of the in-plane and out-of-plane Ru–O bond distances, which matches

well with the negligible variation in the Ru K-edge position. The Debye–Waller factors of the Ru–O shells were estimated to be greater for the Ca-substituted derivative than for the pristine RuSr₂GdCu₂O₈ and the Ba-substituted derivative, cross-confirming a significant enhancement of structural disorder after the Ca substitution.

The present XANES/EXAFS results demonstrate that the replacement of Sr with Ca or Ba makes it possible to control the unit cell dimension of the ruthenocuprate along the *c*-axis and the interlayer distance between the CuO₂ and RuO₂ layers. From the magnetic susceptibility measurement, it becomes clear that the alkaline earth metal substitution does not change the magnitude of magnetic coupling in the RuO₂ layer significantly. In this regard, influence of the internal magnetic field on the superconducting pairs is believed to be tunable by controlling the interlayer distance between both the layers through the substitution. However, the electrical resistance data revealed that there is no systematic correlation between the interlayer distance and *T_c* in the present ruthenocuprates. In particular, an increase of the interlayer distance between the CuO₂ and RuO₂ layers after the Ba substitution should lead to the weakening of the pair-breaking effect of the ordered Ru magnetic moments on the superconducting CuO₂ sheets. However, the *T_c* of the Ba-substituted derivative was found to be even lower than that of the pristine compound, which provides strong evidence on the negligible interplay between the internal magnetic field in the RuO₂ layer and the superconductivity in the CuO₂ layer. Instead, on the basis of the Cu K-edge EXAFS results, we have attributed the observed *T_c* decrease to a slight depletion of hole density. Such a depression of superconductivity was also detected for the Ca-substituted derivative. In this case, the observed variation of *T_c* cannot be explained with the change of the Cu electronic structure, because an increase of the hole density suggested from the shrinkage of Cu–O bond distances should enhance the *T_c* of the present ruthenocuprate having a hole-underdoped state. Moreover, the presence of cation mixing of Cu and Ru in the Ca-substituted compound makes it difficult to estimate the variation in the Cu valency from that in the Cu–O bond length. Although the origin of the *T_c* change caused by the Ca substitution is not very clear at the moment, it seems to be related to the enhancement of structural disorder such as cation mixing, as found from the XRD and EXAFS analyses. Taking into account the fact that structural disordered sites can play a role as a trapping site for itinerant holes in the superconductive CuO₂ layer, increase of the structural disorder would be responsible for the depression of superconductivity in the Ca-substituted derivative. In addition, the variance of the size of alkaline earth metal cations in the rock-salt layers of the substituted derivatives is supposed to perturb the periodic potential and the CuO₂ sheets, which is partly responsible for the observed *T_c* depression upon the Ca or Ba substitution.

Conclusions

We have carried out systematic investigations on the crystal and electronic structures and the physicochemical properties of the alkaline earth metal substituted ruthenocuprates RuSr_{1.9}A_{0.1}GdCu₂O₈ (A = Ca, Sr, and Ba). From structural analyses, we have confirmed that it is possible to control the interlayer distance between the CuO₂ and the RuO₂ layers through the alkaline earth metal substitution and hence to tune the pair-breaking effect of internal magnetic field on the superconductive

CuO₂ layer. However, no systematic relationship between the *T_c* and the interlayer distance/magnetization was observed in the present ruthenocuprates. In this regard, we have concluded that the weak ferromagnetism in the RuO₂ layer has only a negligible effect on the superconducting property of the CuO₂ layer of the ruthenocuprate. Such a weak interaction between the two properties can be explained from the fact that the weak-ferromagnetic coupling due to the canting of Ru moments is mainly oriented along the *ab*-plane and hence the interaction between magnetic moments of RuO₂ layer and the superconducting pairs in the CuO₂ layer along the *c*-axis becomes minimized. This conclusion was further supported by the previous zero-field muon-spin rotation experiment where the magnetic order appeared not to be significantly modified by the onset of the superconductivity due to no significant interaction between the two properties.⁹

Acknowledgment. This work was supported by Korea Research Foundation Grant (KRF-2003-042-C00065) and partly by the SRC/ERC program of MOST/KOSEF (Grant R11-2005-008-03002-0). The experiments at the Pohang Light Source (PLS) were supported in part by MOST and POSTECH.

References and Notes

- (1) Bauernfeind, L.; Wider, W.; Braun, H. F. *Physica C* **1995**, 254, 151.
- (2) Tallon, J. L.; Bernhard, C.; Bowden, M. E.; Gilberd, P. W.; Stoto, T. M.; Pringle, D. J. *IEEE Trans. Appl. Supercond.* **1999**, 9, 1696.
- (3) Williams, G. V. M.; Kramer, S. *Phys. Rev. B* **2000**, 62, 4132.
- (4) Chmaissem, O.; Jorgensen, J. D.; Shaked, H.; Dollar, P.; Tallon, J. L. *Phys. Rev. B* **2000**, 61, 6401.
- (5) Pickett, W. E.; Weht, R.; Shick, A. B. *Phys. Rev. Lett.* **1999**, 83, 3713.
- (6) Nakamura, K.; Freeman, A. J. *Phys. Rev. B* **2002**, 66, 140405.
- (7) McLaughlin, A. C.; Zhou, W.; Attfield, J. P.; Fitch, A. N.; Tallon, J. L. *Phys. Rev. B* **1999**, 60, 7512.
- (8) Jorgensen, J. D.; Chmaissem, O.; Shaked, H.; Short, S.; Klamut, P. W.; Dabrowski, B.; Tallon, J. L. *Phys. Rev. B* **2001**, 63, 054440.
- (9) Bernhard, C.; Tallon, J. L.; Neidermayer, Ch.; Blasius, Th.; Golnik, A.; Brucher, E.; Kremer, R. K.; Noakes, D. R.; Stronach, C. E.; Ansaldo, E. J. *Phys. Rev. B* **1999**, 59, 14099.
- (10) Fainstein, A.; Winkler, E.; Butera, A.; Tallon, J. L. *Phys. Rev. B* **1999**, 60, 12597.
- (11) Tallon, J. L.; Loram, J. W.; Williams, G. W. M.; Bernhard, C. *Phys. Rev. B* **2000**, 61, 6471.
- (12) Pozek, M.; Dulicic, A.; Paar, D.; Williams, G. V. M.; Kramer, S. *Phys. Rev. B* **2001**, 64, 064508.
- (13) Liu, R. S.; Jang, L. Y.; Hung, H. H.; Tallon, J. L. *Phys. Rev. B* **2001**, 63, 212507.
- (14) Hur, S. G.; Park, D. H.; Hwang, S. J.; Kim, S. J.; Lee, J. H.; Lee, S. Y. *J. Phys. Chem. B* **2005**, 109, 9239.
- (15) (a) Mandal, P.; Hassen, A.; Hemberger, J.; Krimmel, A.; Loidl, A. *Phys. Rev. B* **2002**, 65, 144506. (b) Hemberger, J.; Hassen, A.; Krimmel, A.; Mandal, P.; Loidl, A. *Physica C* **2002**, 312–313, 805.
- (16) Choy, J. H.; Hwang, S. J.; Park, N. G. *J. Am. Chem. Soc.* **1997**, 119, 1624.
- (17) Lattice parameters of RuSr_{1.9}Ca_{0.1}GdCu₂O₈: *a* = 3.8372(1) Å, *c* = 11.5609(6) Å, *V* = 170.226(13) Å³. Lattice parameters of RuSr₂GdCu₂O₈: *a* = 3.8374(1) Å, *c* = 11.5735(3) Å, *V* = 170.424(7) Å³. Lattice parameters of RuSr_{1.9}Ba_{0.1}GdCu₂O₈: *a* = 3.8395(1) Å, *c* = 11.5872(4) Å, *V* = 170.818(9) Å³.
- (18) Shannon, R. D. *Acta Crystallogr., Sect. A: Cryst. Phys., Diff., Theor. Gen. Crystallogr.* **1976**, 32, 751.
- (19) Choy, J. H.; Kim, D. K.; Hwang, S. H.; Demazeau, G. *Phys. Rev. B* **1994**, 50, 16631.
- (20) The best-fitted residual *F*² factor ($=\sum\{k^3(\chi(k)_{\text{cal}} - \chi(k)_{\text{exp}})\}^2/(n - 1)$) was determined to be 0.026 for RuSr₂GdCu₂O₈, 0.038 for RuSr_{1.9}Ca_{0.1}GdCu₂O₈, and 0.047 for RuSr_{1.9}Ba_{0.1}GdCu₂O₈.
- (21) The best-fitted residual *F*² factor ($=\sum\{k^3(\chi(k)_{\text{cal}} - \chi(k)_{\text{exp}})\}^2/(n - 1)$) was determined to be 0.039 for RuSr₂GdCu₂O₈, 0.036 for RuSr_{1.9}Ca_{0.1}GdCu₂O₈, and 0.043 for RuSr_{1.9}Ba_{0.1}GdCu₂O₈.